

One-dimensional modeling methodology for shock tubes: Application to the EAST facility

Maitreyee P. Sharma*, Alessandro Munafò†, Marco Panesi‡

University of Illinois at Urbana-Champaign, Urbana,, IL 61801, USA

Aaron M. Brandis, Brett A. Cruden,§

AMA at NASA Ames Research Center, Moffett Field, CA, 94035, USA

In this work, a one-dimensional methodology for simulating shock tubes is developed. The model accounts for the viscous interactions of the shock with the shock tube wall by adding an area change source term in the 1-D conservation equations corresponding to the boundary layer growth. This source term corresponds to the mass and energy going into the boundary layer. The boundary layer growth is computed using a simple model with a scaling factor. This scale factor is used to tailor a solution to match the deceleration profile of a shock tube test. In doing so, not only will the source term take into account boundary layer losses, it will also cover any effect due to radiative cooling losses from the gas. For this study, the Electric Arc Shock Tube(EAST) facility at NASA Ames Research Center is modeled for Earth reentry conditions. The purpose of this paper is to investigate if anomalies identified for certain conditions in the EAST data are due to shock deceleration. These anomalies include measuring electron number density above equilibrium predictions and observing that radiance profiles can continually increase behind the shock, never reaching steady state, for certain shots (typically those less than 10 km/s). An eleven species air mixture is chosen to study the chemistry of the flow. Comparisons of the simulations to the experimental results are presented. Good agreement with the shock deceleration profiles was achieved by tuning in the boundary layer scale factor. The temperature as well as electron number density increases behind the shock, as has also been observed in the experiments. Finally, radiance comparisons between results from NEQAIR and experiments also show good agreement for some shots, but significant discrepancies are still observed for others.

Nomenclature

δ	= Boundary layer thickness (mm)
ϵ	= Area change coefficient (dimensionless)
μ	= Kinematic viscosity (m^2/s)
ω_i	= Species 'i' kinetic source term ($\text{kg}/\text{m}^3\text{s}$)
Ω_{DE}	= Dissociation energy source term (J/kgs)
Ω_{TE}	= Translation-Electronic energy relaxation source term (J/kgs)
Ω_{VE}	= Vibration-Electronic energy source term (J/kgs)

*Graduate Research Assistant, Department of Aerospace Engineering, University of Illinois at Urbana-Champaign, 306 Talbot Lab, 104 S. Wright St., Urbana, 61801, IL, USA

†Post Doctoral Research Associate, Department of Aerospace Engineering, University of Illinois at Urbana-Champaign, 306 Talbot Lab, 104 S. Wright St., Urbana, 61801, IL, USA

‡Assistant Professor, Department of Aerospace Engineering, University of Illinois at Urbana-Champaign, 306 Talbot Lab, 104 S. Wright St., Urbana, 61801, IL

§Sr. Research Scientists, Aerothermodynamics Branch, NASA Ames Research Center, CA, 94035, USA, AIAA Associate Fellows

Ω_{VT}	= Vibration-Translation energy relaxation source term (J/kgs)
ρ	= Total density (kg/m ³)
ρ_i	= Species 'i' density (kg/m ³)
A	= Area (m ²)
E	= Total energy (J/kg)
e_{ve}	= Electronic-Vibration Energy (J/kg)
h	= Specific enthalpy (J/kg)
k	= Boundary layer thickness scaling factor (dimensionless)
p	= Pressure (Pa)
R	= Shock tube radius (m)
t	= Time (s)
t_{arr}	= Shock arrival time (s)
u	= Flow velocity (m/s)
x	= Distance along the shock tube (m)

I. Introduction

Hypersonic entry into the Earth atmosphere is characterized by velocities ranging between 8 and 13 km/s. The values of a typical Lunar return mission are around 10-11 km/s. At these high speeds of reentry, a large portion of the heat-flux experienced by spacecraft is due to radiation. The intense radiative heating is caused by strong radiators such as atomic N and O, which are produced as a result of the dissociation of O₂ and N₂ in the shock layer. In numerical simulations, the abundance of each of these radiator species, during Earth entry, are determined based on chemical kinetics models which are developed and validated using experiments. The kinetics not only affect the radiative heating but also have a significant impact on the convective heating.³

In the experiments carried out in the EAST facility, it is observed that the shock decelerates along the length of the tube.⁴ This shock deceleration occurs due to the viscous interaction between the shocked gas and the shock tube wall. Another source of shock deceleration is radiation at high shock speeds, which causes the flow to lose energy. Obtaining an accurate description of the chemical kinetic data from the shock tube necessitates an accurate description of the development of the shock, thereby, making it important to model the shock-boundary layer interactions. Previous attempts have been made to study the effect of shock deceleration due to boundary layer interactions. Light⁵ compared unsteady flow simulations with shock deceleration to experimental data. In that work, Light imposed appropriate boundary conditions which depended both on the deceleration of the shock and the mass loss into the boundary layer. The frame of reference was fixed to the decelerating shock. The unsteady nature of the flow with shock deceleration was further simplified by modeling the system as a series of independent, one dimensional, steady stream tube systems each consisting of fluid elements shocked at different speeds.

The purpose of this work is the development of a computational tool for the modeling of the flow in a shock tube facility for various planetary entry conditions. Viscous effects are incorporated by a phenomenological model used to describe the boundary layer growth. The predicted flow properties (*e.g.*, chemical composition and temperatures) are used to compute the optical properties of the plasma (*e.g.*, radiance) and compared against experiments in order to validate the chemical kinetic models.

This paper is structured as follows. The experimental setup is briefly described in Section II. Section III describes the mathematical modelling implemented in this work. Results are reported in Section IV. Section V reports the concluding remarks and provides an outline of the future work.

II. Electric Arc Shock Tube

The EAST facility set up has been described in previous papers.⁴ In summary, the driven tube is made of aluminum with a diameter of 10 cm. A stainless steel diaphragm separates it from the driver section. The driver is pressurized with 200 psi of Helium. The driver gas is heated by an electric arc delivered by the 863 μ F capacitor bank which is charged to a voltage depending on the desired velocity. The arc increases the temperature and pressure in the driver section rupturing the diaphragm and initiating a shock wave. The shock locations are tracked downstream by piezoelectric transducers placed along the walls of the shock tube. The data from these transducers is used to obtain the x-t diagram of the shock. These plots are compared

to the x-t diagrams obtained from the simulations. About 7.5 m downstream of the diaphragm, the optics of four spectrometers focus on a 12.5 cm long test section. The four spectrometers are enclosed in vacuum chambers and have ranges varying from vacuum ultraviolet to mid infrared. The data recorded from these spectrometers is compared to the radiance obtained from the simulations.

The driven gas composition used in the present study emulates the composition of the Earth atmosphere. The Earth atmosphere is modeled using 11 air species mixture with an initial driven gas composition of 79% N₂ and 21% O₂ by volume. The test conditions used in the simulations are described in the results section.

III. Physical modeling

In order to study the effects of boundary layer growth on the shock speed attenuation, the one-dimensional flow governing equations are modified by introducing an area change source term (*i.e.*, quasi one-dimensional flow). The area change depends on the boundary layer growth in order to account for the mass loss into the wall boundary layer.

This section describes the governing equations for the shock tube flow simulations. In order to obtain the area source term it is necessary to choose an appropriate model for the boundary layer growth. The description of the boundary layer modeling is provided in the following subsection. Finally, the numerical schemes and flow solver code used for the simulations are described.

A. Governing equations

The conservation law form of the governing equations for a quasi-one-dimensional non-equilibrium flow read:

$$\frac{\partial}{\partial t} \begin{pmatrix} \rho_i \\ \rho u \\ \rho E \\ \rho e_{ve} \end{pmatrix} + \frac{\partial}{\partial x} \begin{pmatrix} \rho_i u \\ (\rho u^2 + p) \\ u(\rho E + p) \\ u(\rho e_{ve} + p) \end{pmatrix} = \begin{pmatrix} \omega_i - \epsilon \rho_i u \\ -\epsilon \rho u^2 \\ -\epsilon u(\rho E + p) \\ \Omega_{VT} + \Omega_{TE} + \Omega_{VE} + \Omega_{DE} \end{pmatrix}, \quad (1)$$

where the area change coefficient, ϵ , is given by:

$$\epsilon = \frac{1}{A} \frac{\partial A}{\partial x}. \quad (2)$$

The subscript i represents the different chemical species present in the flow. In modeling chemistry of the shock tube experiments, there are a total of 12 species which include 11 species air mixture and the driver gas, Helium.

The modified equations have source terms due to change in the area in all three conservation equations. The second source term in the continuity equation represents the mass efflux from the control volume into the boundary layer. There is a source of energy loss in the energy conservation equation as well.

B. Boundary layer modeling

Due to dissipation into the boundary layer, the effective area behind by the shock is given by:

$$A = \pi(R - \delta)^2, \quad (3)$$

where the symbols R and δ stand for the tube radius and the boundary layer thickness respectively. The area change coefficient, ϵ , is obtained via the substitution of Eq. (3) in Eq. (2):

$$\epsilon = \frac{1}{A} \frac{\partial A}{\partial x} = \frac{-2}{R - \delta} \frac{\partial \delta}{\partial x}. \quad (4)$$

The above relation necessitates an expression for the boundary layer growth. In the present work, the following model is adopted:⁶

$$\delta \frac{\partial \delta}{\partial t} = \frac{\beta^2}{2}, \quad (5)$$

where the β parameter depends on the kinematic viscosity and can be evaluated from the boundary layer profile. For a constant value of β , Eq. (5) can be immediately integrated to give:

$$\delta = \beta \sqrt{t - t_{\text{arr}}(x)}, \quad (6)$$

where quantity $t_{\text{arr}}(x)$ stands for the shock arrival time. The former quantity is a function of location and, implicitly, of time as well, and must be continuously updated during the calculation. A reasonably approximation for the β parameter may be obtained from the velocity profile as:⁶

$$\beta = 4\sqrt{\frac{\mu}{\rho}}. \quad (7)$$

C. Numerical method

The quasi 1-D model developed in the previous subsections is coupled with the flow solver, HEGEL (High fidelity tool for maGnEtogas-dynamic appLIcations). The solver uses PETSC(Portable, Extensible Toolkit for Scientific Computation)⁷⁻⁹ to solve the system of partial differential equations. The flow solver is coupled with a chemical and thermodynamic library, PLATO (PLASmas in ThermOdyanmic non-equilibrium). It can therefore be used to study chemically reacting flows. The flow solver is further described by Munafò et al.¹⁰

The spatial discretization is obtained using the finite volume method.¹¹ The inviscid fluxes are computed using the Monotone Upstream Centered Scheme for Conservation Laws (MUCSCL) technique proposed by van Leer.¹² The space-discretized set of equations is integrated in time using an explicit scheme with point implicit treatment of the sources and the fluxes.

For the calculations of the boundary layer thickness, shock arrival times are required. These are a function of both time and space and correspond to the time when a particular fluid particle is first shocked. Hence, to record the shock arrival times, a Lagrangian approach is used where individual fluid particles and their flow properties are tracked. The value of the boundary layer thickness is then linearly interpolated onto the grid nodes. The results of the simulations are compared against the Euler case, with no shock deceleration. These simulations correspond to a case with boundary layer thickness set to zero.

IV. Results

The simulations are run at the conditions encountered during re-entry into the Earth atmosphere. The driven gas is a mixture containing 79% N₂ and 21% O₂. The driven gas is at a temperature of 300 K and the pressure in the driven section is set to 0.2 Torr (26.6 Pa) initially. The driver gas is 100% He. The simulations are quasi 1-D. The thermochemistry model for the simulations is the two-temperature Park model¹³ where the vibrational levels of the molecules are at equilibrium at a temperature T_v whereas the translational temperature is T . The reaction rates computed by Park¹³ are being used to compute the chemical source terms.

The simulations take approximately 48-50 hours for the shock to travel 8.25m downstream of the diaphragm using 32 intel processors. The simulation time can be further reduced by increasing the number of processors being used.

A. Grid Independence Study

A grid independence study is performed for the non-decelerating case, i.e. Euler simulation. Three element sizes are considered, 1 mm, 0.5 mm and 0.2 mm. The length of the shock tube simulated for the grid independence study is 2.5m. Figure 1a shows the x-t diagram of the shock and figure 1b is the velocity profile. The initial driver temperature is set to 10,000 K. As seen the velocity remains constant after an initial drop. This drop in the velocity is due to the instantaneous removal of the diaphragm which initially causes a large shock speed due to acute gradients of the flow properties across the shock. After the initial drop, figure 1 shows that the simulations are grid converged. The shock velocities are within a range of ± 0.003 km/s of each other.

B. Boundary Layer Growth

This next study focuses on the modeling of the boundary layer growth. A simplified theoretical model is used to obtain the boundary layer growth as described in Section IIIB. The deceleration observed with this model is very low. Hence, a scaling factor is used to match the shock deceleration profile with those of the experiments. This is shown in equation (8). The boundary layer growth directly affects the shock speed. The deceleration study is based on the Earth atmosphere conditions during re-entry.

$$\delta = k\beta\sqrt{t - t_{\text{arr}}(x)}, \quad (8)$$

Figure 2 shows the effect of various scaling factors on the shock deceleration profiles. As expected, higher scaling factor results in more shock deceleration since the boundary layer is thicker as seen in figure 3. The larger boundary layer thickness results in an increase in the area source term as seen in equation (4). A scaling factor of zero corresponds to the inviscid case with no boundary layer which corresponds to the Euler simulation and hence as expected the shock speed remains constant as seen in the previous subsection.

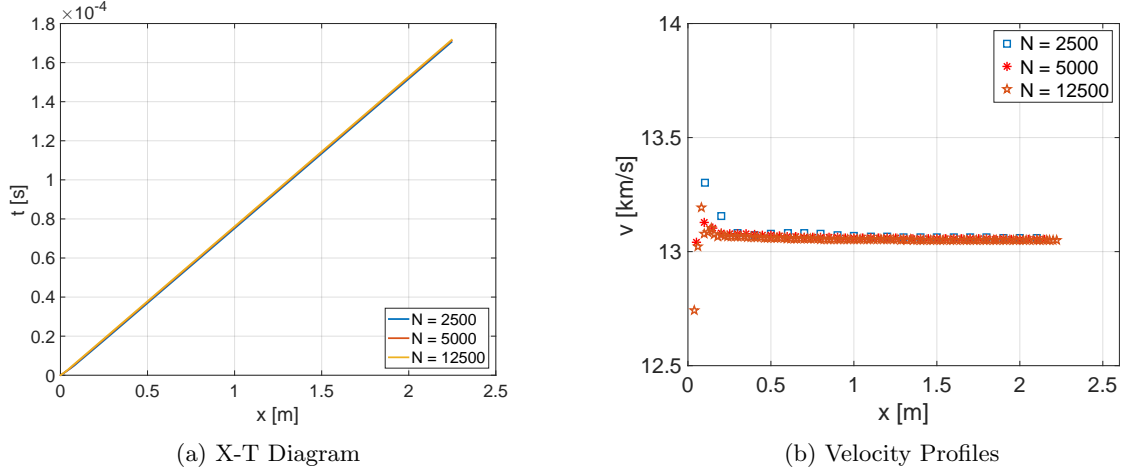


Figure 1: Grid independence study

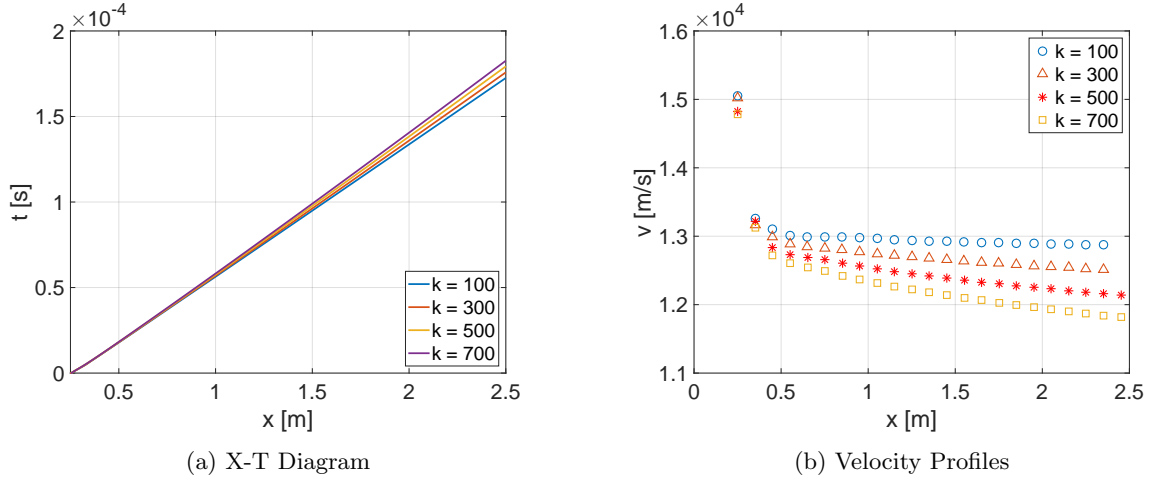


Figure 2: Effect of Boundary Layer Growth on the Shock Speed

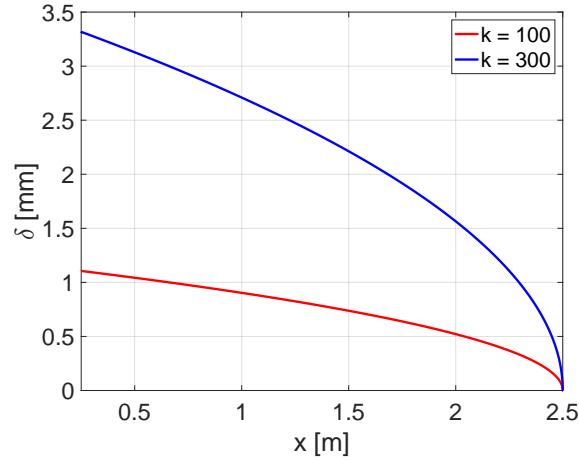


Figure 3: Boundary layer thickness for different k values

C. Modeling of Flow in the Shock Tube

For the flow simulations, the driver gas temperature is set to 10,000 K. Figure 4, shows a comparison of the velocity profiles of the inviscid simulation and viscous simulation. The decelerating (viscous) case corresponds to a scaling factor (k) of 1000. The shock speed in the inviscid case is 11.03 km/s and remains constant throughout the shock tube. Various flow quantities are compared for the two simulations at the point of intersection of the velocity profiles to provide a quantitative analysis of the effect of shock deceleration.

A comparison is made between the species concentration within the shock obtained from the simulations (solid line) and their equilibrium concentrations (dashed line) within the shock at the same temperature and pressure in figure 5a. These equilibrium compositions are obtained using the incident shock equilibrium option from CEA.¹⁴ This comparison shows that the gas mixture within the shock is in thermal and chemical non-equilibrium due to shock deceleration since the temperature behind the shock increases. This affects the radiance of the system and therefore should be accounted for when the shock tube is used to investigate gas phase reactions and obtain chemical reaction rates.

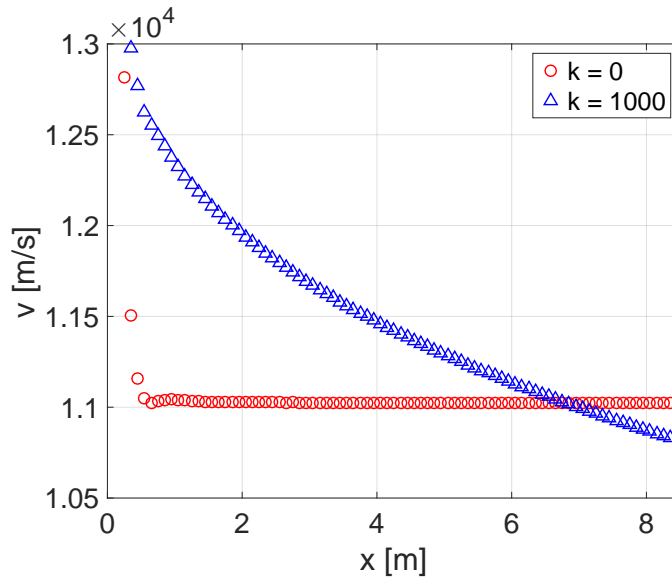
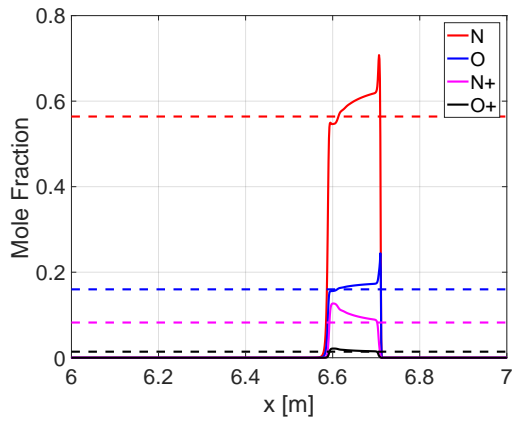
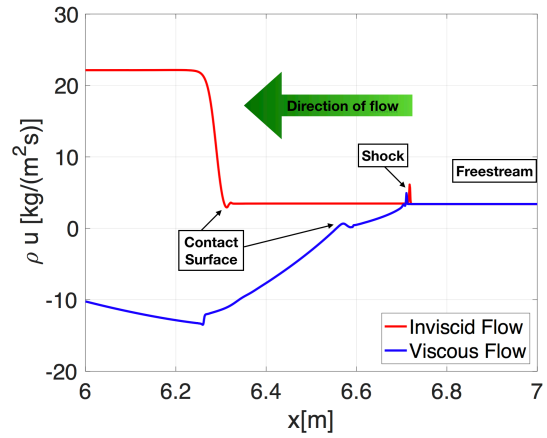


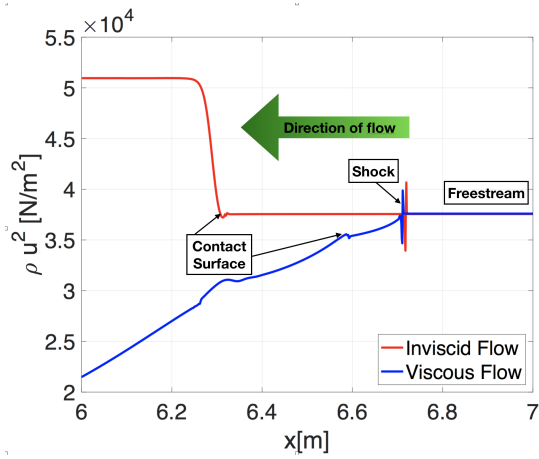
Figure 4: Comparison of shock velocity profile



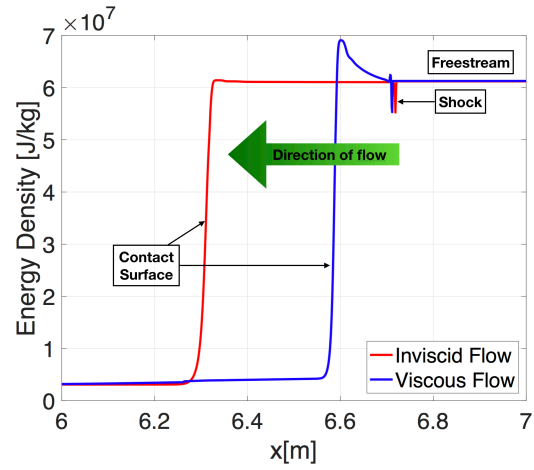
(a) Species composition; CEA(Dashed Line), Viscous(Solid Line)



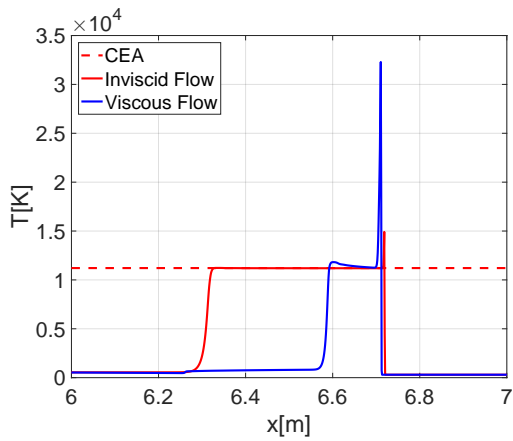
(b) Mass Flux across the shock



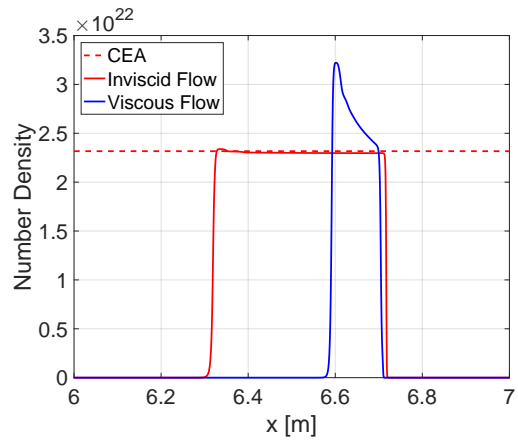
(c) Momentum Flux across the shock



(d) Energy Density across the shock



(e) Temperature behind the shock



(f) Electron number density

Figure 5: Comparison of Results with the Inviscid Solution at a shock speed of 11 km/s

The Rankine-Hugoniot jump conditions across a shock wave conserve mass, momentum and energy.

These jump conditions are represented by the following three equations:

$$\begin{aligned}\rho_1 u_1 &= \rho_2 u_2 \\ \rho_1 u_1^2 + p_1 &= \rho_2 u_2^2 + p_2 \\ h_1 + \frac{1}{2} \rho_1 u_1^2 &= h_2 + \frac{1}{2} \rho_2 u_2^2\end{aligned}$$

Mass, momentum and energy are conserved across the shock for inviscid flows. This is represented by the solid red lines in figures 5b - 5d. These are compared with simulations of the decelerating shock wave at the same shock speed at the test section. These shock tube simulations show a decrease in the mass flux and the momentum flux across the shock when viewed in the direction of the flow in the shock relative frame. This mass source term corresponds to the mass being lost to the wall boundary layer. There is a decrease in the momentum flux across the shock as well corresponding to the mass loss. It is noticed that the energy density increases along the length of the shock tube in the flow direction in the shock relative frame. This results in the temperatures increasing behind the shock which has also been observed in the experiments.¹⁵

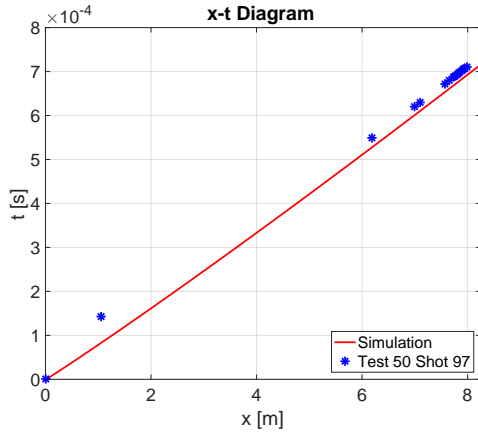
The distance between the contact surface and the shock front is larger in the inviscid flow (no deceleration) when compared to the viscous flow. This happens because the contact surface decelerates slower than the shock in viscous flow.¹⁶

As expected from the energy flux profile, figure 5e shows that the temperature just behind the shock front is the same as the inviscid case and the equilibrium post shock temperature as calculated using CEA software. However, the temperature of the viscous simulations increases behind the shock front since the gas behind the shock front was shocked at higher speeds and hence, their temperatures correspond to the equilibrium temperatures for those shock speeds. This increase in temperature behind the shock front also lead to an increase in the electron number density with the shock as depicted in figure 5f.¹⁷ At such high speeds, the increase in the electron number density is not observed in the experiments. Due to radiation losses occurring in experiments, the temperature behind the shock decreases negating the effect of shock deceleration. However, in this work, the radiation losses are not accounted for.

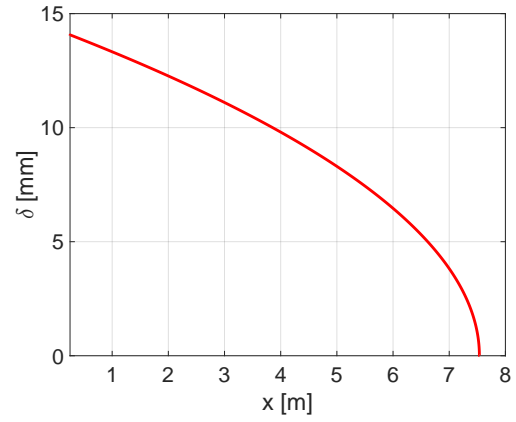
D. Comparison to EAST Experiment

Figure 6 shows a comparison of the simulations results ($k = 1000$) with that of the experiments. The simulation shock speed in the viscous case is around 10.8 km/s in the test section which is the same as the experimental data corresponding to EAST Test 50 Shot 97.¹⁸ Small differences in the shock speed profiles can lead to substantial differences in the radiation profiles. In future work, this can be further improved by tuning the scaling factor and possibly using a variable scaling factor. Figure 6b show the boundary layer thickness in the test section. The boundary layer for $k = 1000$ starting at an initial driver temperature of 10,000 K has a thickness of 14 mm in the test section. This thickness is expected to be significantly larger than what would be found in experiment. As the simulations do not account for radiative losses, and do not model the imperfections of the tube walls or optical access ports, all of which would cause the shock to decelerate more, this thickness should be considered an upper bound. The x-t diagrams of the simulations and experiments show some variations. However, extracting the shock deceleration profiles show a good match with the experiments as seen in figures 6c and 6d.

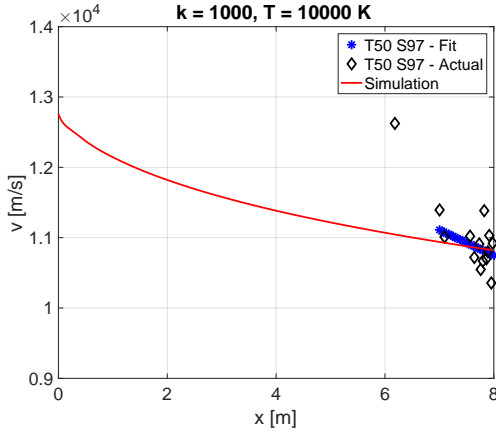
In order to compare the radiance to that of the experiments, NEQAIR¹⁹ is used. NEQAIR is a line-by-line radiation code which stands for Nonequilibrium Air Radiation. The radiance comparisons in this paper represent the set of NEQAIR calculations with a spatial convolution. The convolution functions account for finite spatial resolution in the experiments and depend upon the experiment set up.¹⁵ A meaningful comparison with the experiments is achieved by convolving the simulation results with functions which are determined for each shot conducted at the EAST facility. Two EAST Shots are used for the radiation comparisons. First being EAST Test 50 Shot 97 with a shock speed of 10.8 km/s. This is compared to the viscous case stated above with a k of 1000.



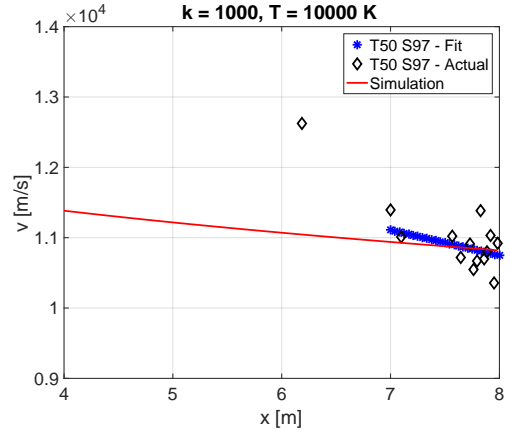
(a) Comparison of x-t Diagram



(b) Boundary Layer Thickness in the Test Section



(c) Comparison of Shock Velocity Profiles



(d) Comparison of Shock Velocity Profiles - Zoomed

Figure 6: Comparison of results from the simulations and experiments, $k = 1000$, $T_{\text{driver}} = 10000$ K

Figures 7b-7d show the radiation comparisons for various wavelength regions of the convolved NEQAIR calculations with the experiment. The increasing x-axis represents the region upstream behind the shock. In the IR and Red region there is significant difference between the experiment and simulation. This may be attributed to the fact that the deceleration profile of the shot and simulations do not match exactly. Future work simulations will address fine tuning the k value to provide better agreement for the shock deceleration. However, the comparisons in the UV region show very good agreement quantitatively. While in the VUV region, the results have similar trends and the experimental observations are close to the values obtained from the simulation. The increasing radiance behind the shock is captured by the simulation which is due to the increase in temperature and electron number density behind the shock front.

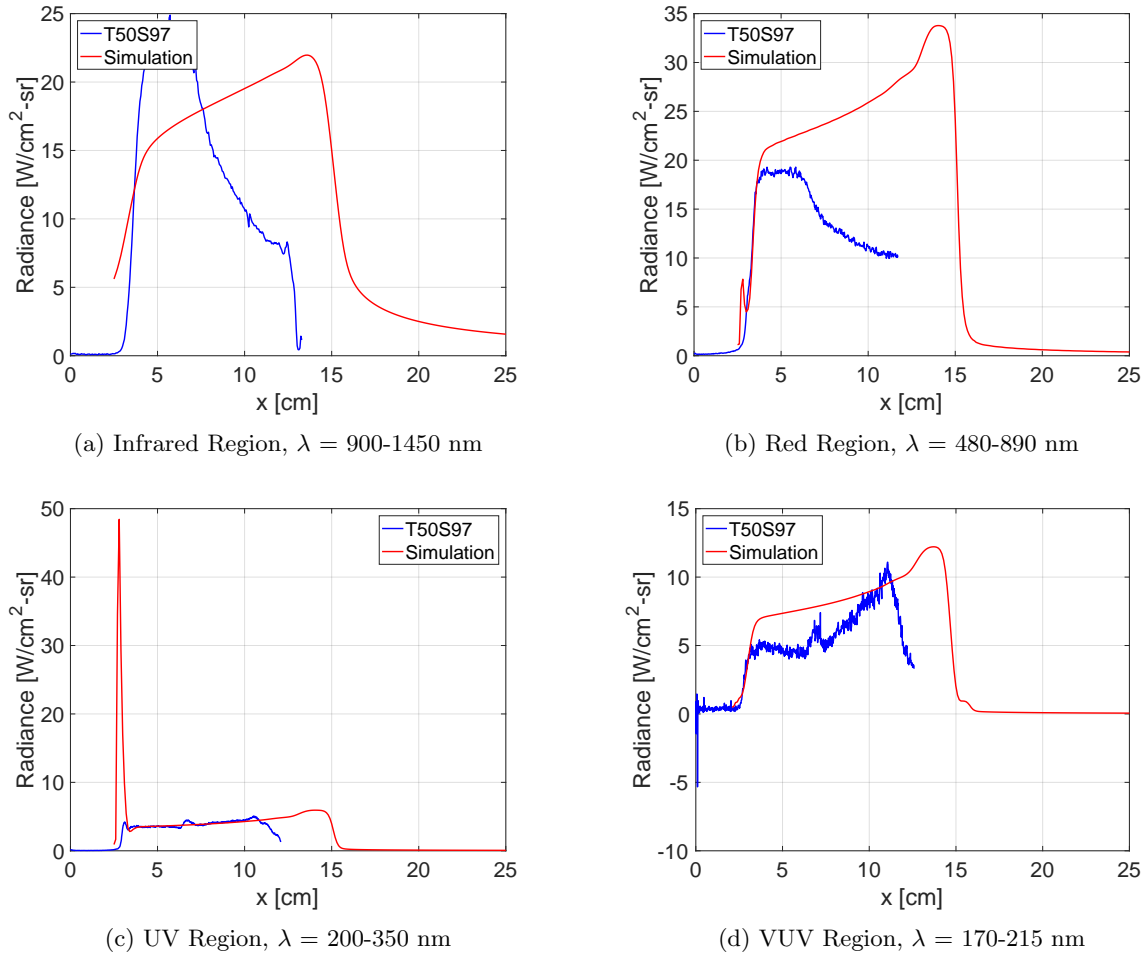
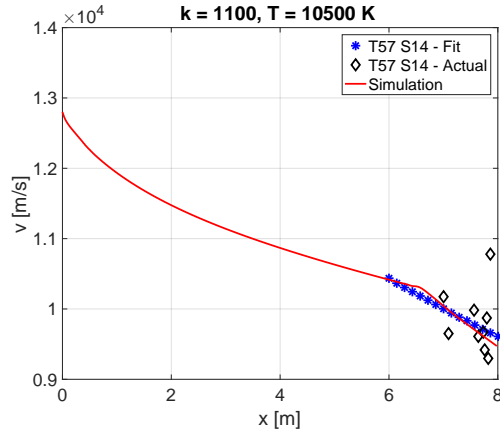


Figure 7: Radiance Comparison for Test 50 Shot 97

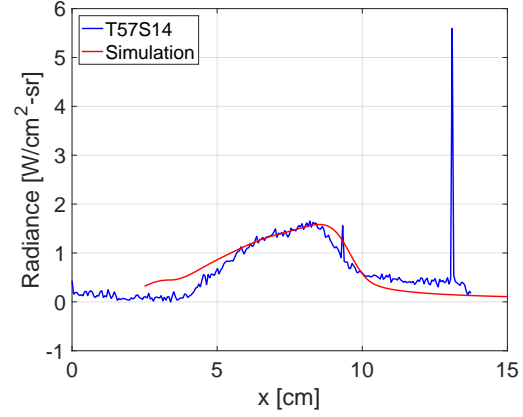
The second EAST test that is considered is Test 57 Shot 14 having a shock speed of 9.5 km/s in the test section. For the simulation, the initial driver temperature is 10,500 K with a ‘k’ of 1100. The higher scaling factor achieves lower shock speed in the test section. A comparison of the radiance is made at a shock location of 7.75 m downstream of the diaphragm where the shock speed is 9.72 km/s.

The shock deceleration profiles are compared in figure 8a. The simulation shows a deflection in the shock speed. This is suspected to be a numerical artifact due to using a high time step of 0.1 ns. For the high speed simulations with non-equilibrium presented in this paper, a time step of typically 0.05 ns is used. However, the velocity profiles match well in the test section.

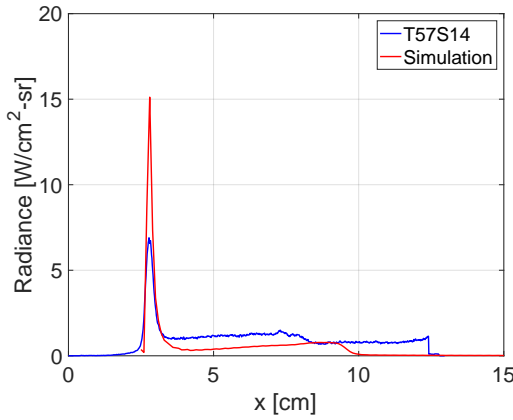
Figures 8b-8d shows that the experiments record an increase in the radiation behind the shock which is captured by the viscous simulation. This increase in radiance is due to the fact that the temperature behind the shock front increases as the gas further away from the shock was shocked at a higher velocity. In the IR region, there is no steady state radiance as can be seen from the figures. Hence, using this model can potentially provide an avenue to understand the data obtained from the experiments. There is a dramatic increase in the radiance in the IR region when compared to the UV region in the EAST data which is also observed in the simulations. The radiance data in the VUV region shows that it is steady. The simulations show radiance increase in this region as well.



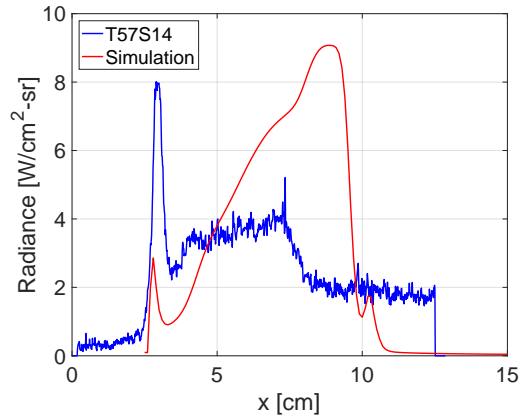
(a) Comparison of Shock Velocity Profiles



(b) Infrared Region, $\lambda = 1130-1700$ nm



(c) UV Region, $\lambda = 200-350$ nm



(d) VUV Region, $\lambda = 130-176$ nm

Figure 8: Radiance Comparison for Test 57 Shot 14

It can therefore be concluded from the results presented that the model developed in this paper is capable of modeling the shock deceleration and its effects on the flow field qualitatively. The agreement between the experiments and simulations can further be improved by studying the scaling factor and reproducing the deceleration profiles of the experiments more accurately. However, this study can be used to explain the anomalies in some of the EAST tests, which sometimes show the increasing radiance profiles could be due to shock deceleration. For more definitive results, the deceleration profile of each EAST test requires refinement, and a large selection of shots and conditions would be required to analyze.

V. Conclusions

The aim of this work is to develop an accurate quick computation tool to simulate the flow in the shock tube with an application to the EAST facility at NASA Ames Research Center. The requirement of such a model arises since the different tests are run every day in the experimental facility which need to be simulated individually since each shot may have differing decelerations. Therefore, a quasi 1-D model is developed and coupled with the flow solver, HEGEL, to simulate the shock tube flows. The composition of gas mixture in the driven section represents the composition of the Earth atmosphere with 11 species and in the future will also be used to study the shock tube experiments conducted for the Martian atmosphere.

The simulations account for the boundary layer mass, momentum and energy loss by introducing an area change source term in the conservation equations. This mass loss leads to attenuation of the shock speed. Since the particles behind the shock are shocked at different speeds, the temperature behind the shock increases as a result of the shock deceleration leading to deviation from a 1-D Euler-type relaxation. The

increasing electron number density and temperature behind the shock lead to an increase in the radiance which is also captured by the simulations. All simulations are compared to an inviscid solution for the same speed, which produces a steady relaxation towards equilibrium following the Rankine-Hugoniot jump conditions.

The results from the simulations are finally compared with the experimental results. For some combinations of spectral region and condition, these results show reasonable agreement with experimental observations. The temperature profiles showcase behavior similar to the experiments carried out in the EAST facility. As a final comparison, the radiance from the experiments is compared to those obtained from the simulations. NEQAIR is used to calculate the radiance from the simulation data using appropriate convolution functions. These comparisons lead to the conclusion that the model developed in this work is capable of simulating the trends observed in experiments, however, further simulations and analysis are required to accurately reproduce the experimental results.

Therefore, in the future, the authors would like to study the scaling factor further and implement an adaptive scaling factor which will be based on the deceleration profiles obtained from experiments. The model would further be improved by taking into account radiation losses that occur in the flow.

VI. Acknowledgments

This work was supported by Analytical Mechanics Associates Inc. Summer Internship Program at NASA Ames Research Center.

References

- ¹Cruden, B. A., Brandis, A. M., White, T. R., Mahzari, M., and Bose, D., "Radiative heating during mars science laboratory entry: Simulation, ground test, and flight," *Journal of Thermophysics and Heat Transfer*, 2016, pp. 642–650.
- ²Brandis, A. M., Cruden, B. A., White, T. R., Saunders, D. A., and Johnston, C. O., "Radiative heating on the after-body of Martian entry vehicles," *45th AIAA Thermophysics Conference*, 2015-3111.
- ³Hollis, B. R. and Prabhu, D. K., "Assessment of laminar, convective aeroheating prediction uncertainties for Mars-entry vehicles," *Journal of Spacecraft and Rockets*, Vol. 50, No. 1, 2013, pp. 56–68.
- ⁴Cruden, B., Martinez, R., Grinstead, J., and Olejniczak, J., "Simultaneous vacuum-ultraviolet through near-IR absolute radiation measurement with spatiotemporal resolution in an electric arc shock tube," *41st AIAA Thermophysics Conference*, 2009-4240.
- ⁵Light, G., "Test gas properties behind a decelerating shock wave in a shock tube," *The Physics of Fluids*, Vol. 16, No. 5, 1973, pp. 624–628.
- ⁶Bird, R. B., Stewart, W. E., and Lightfoot, E. N., *Transport phenomena*, John Wiley & Sons, 2007.
- ⁷Balay, S., Abhyankar, S., Adams, M. F., Brown, J., Brune, P., Buschelman, K., Dalcin, L., Eijkhout, V., Gropp, W. D., Kaushik, D., Knepley, M. G., May, D. A., McInnes, L. C., Mills, R. T., Munson, T., Rupp, K., Sanan, P., Smith, B. F., Zampini, S., Zhang, H., and Zhang, H., "PETSc Web page," <http://www.mcs.anl.gov/petsc>, 2018.
- ⁸Balay, S., Abhyankar, S., Adams, M. F., Brown, J., Brune, P., Buschelman, K., Dalcin, L., Eijkhout, V., Gropp, W. D., Kaushik, D., Knepley, M. G., May, D. A., McInnes, L. C., Mills, R. T., Munson, T., Rupp, K., Sanan, P., Smith, B. F., Zampini, S., Zhang, H., and Zhang, H., "PETSc Users Manual," Tech. Rep. ANL-95/11 - Revision 3.9, Argonne National Laboratory, 2018.
- ⁹Balay, S., Gropp, W. D., McInnes, L. C., and Smith, B. F., "Efficient Management of Parallelism in Object Oriented Numerical Software Libraries," *Modern Software Tools in Scientific Computing*, edited by E. Arge, A. M. Bruaset, and H. P. Langtangen, Birkhäuser Press, 1997, pp. 163–202.
- ¹⁰Munafò, A., Venturi, S., Macdonald, R. L., and Panesi, M., "State-to-State and reduced-order models for recombination and energy transfer in aerothermal environments," *54th AIAA Aerospace Sciences Meeting*, 2016-0505.
- ¹¹Hirsch, C., *Numerical computation of internal and external flows: The fundamentals of computational fluid dynamics*, Butterworth-Heinemann, 2007.
- ¹²Van Leer, B., "Towards the ultimate conservative difference scheme," *Journal of Computational Physics*, Vol. 135, No. 2, 1997, pp. 229–248.
- ¹³Park, C., "Review of chemical-kinetic problems of future NASA missions. I-Earth entries," *Journal of Thermophysics and Heat transfer*, Vol. 7, No. 3, 1993, pp. 385–398.
- ¹⁴McBride, B. J. and Gordon, S., "Computer Program for Calculation of Complex Chemical Equilibrium Compositions and Applications II. Users Manual and Program Description. 2; Users Manual and Program Description," 1996.
- ¹⁵Cruden, B. A., Brandis, A. M., and Prabhu, D. K., "Compositional dependence of radiance in CO₂/N₂/Ar systems," *44th AIAA Thermophysics Conference*, 2013-2502.
- ¹⁶Mirels, H. and Braun, W., "Nonuniformities in shock-tube flow due to unsteady-boundary-layer action," 1957.
- ¹⁷Cruden, B. A., "Electron density measurement in reentry shocks for lunar return," *Journal of Thermophysics and Heat Transfer*, Vol. 26, No. 2, 2012, pp. 222–230.
- ¹⁸Brandis, A. M. and Cruden, B. A., "Benchmark Shock Tube Experiments of Radiative Heating Relevant to Earth Re-entry," *55th AIAA Aerospace Sciences Meeting*, 2017-1145.

¹⁹Cruden, B. A. and Brandis, A. M., “Updates to the NEQAIR Radiation Solver,” 2014.